

Tunable, Nucleation-Driven Stochasticity in Nanoscale Silicon Oxide Resistive Switching Memory Devices

Tímea Nóra Török,¹ János Gergő Fehérvári,¹ Gábor Mészáros, László Pósa, and András Halbritter*Cite This: <https://doi.org/10.1021/acsanm.2c00722>

Read Online

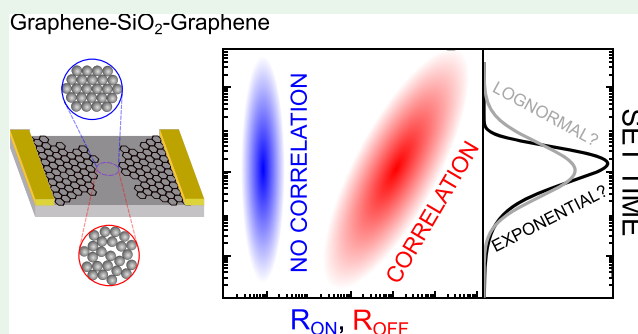
ACCESS |

Metrics & More

Article Recommendations

ABSTRACT: Resistive switching memory devices hold extensive possibilities for realizing artificial neural networks along with nonconventional computing paradigms. Studying and understanding phenomena arising at single resistive switching elements is necessary for utilizing their particular traits for computation. Tuning the variability of the set time—the timespan before the onset of the transition from a high-resistance OFF state to a low-resistance ON state—is key for making use of the inherently stochastic nature of the resistance switching effect. Here, we study the set time statistics in nanometer-sized graphene–SiO_x–graphene resistive switching memory devices. For dedicated OFF state configurations, we demonstrate a universal variance of the logarithmic set time values, which is characteristic to a nucleation-driven crystallization process. Furthermore, we observe clear correlation between the OFF state resistance and the set time, and hence we explore the tunability of the set time statistics via changing the reset amplitude parameter in sequential pulsed measurements. The latter phenomenon could prove useful for controlling stochasticity in memristor-based probabilistic computing applications via the control of the active volume's nanostructure.

KEYWORDS: resistive switching memory, phase change memory, silicon oxide, graphene nanogap, memristor, nucleation



INTRODUCTION

The functionality of von Neumann architectures meets limitations due to the restricted bandwidth of data transfer between processing and memory units. Resistive switching memories serve as building blocks for non-von Neumann computing schemes, which overcome this bottleneck via the implementation of artificial neural networks (ANNs) at the hardware level.^{1,2} Recently, large networks were built of 10⁵–10⁶ artificial synapses, which have shown ~100 times greater energy efficiency and increased speed by a factor of ~100, compared to state-of-the-art GPU-based approaches.^{3,4} Besides accelerating deep neural networks or image processing via convolution,⁵ there are further opportunities that utilize the dynamics of resistive switching memory elements. Their stochastic nature could be a resource in the hardware-level solution of certain NP-hard optimization problems such as graph segmentation^{6,7} or prime factorization.⁸ These resistive switching networks are not only providing fundamentally new computing architectures but are also well fitted to conventional complementary metal–oxide–semiconductor (CMOS) technologies, thereby promising near-future fast and energy-efficient information processing applications.

Resistive switching phenomena are realized in various material systems, relying on fundamentally different physical

mechanisms. These include bipolar filamentary resistive switching due to valence change mechanism (VCM) in transition-metal-oxide systems, electrochemical metalization (ECM) in various material systems,⁹ or phase change memories (PCMs)¹⁰ exhibiting a local, voltage-induced transition between crystalline metallic and amorphous insulating phases. One of the most well-known dielectrics, silicon oxide, also exhibits promising resistive switching properties offering superior compatibility and integrability in CMOS technologies¹¹ and beneficial properties for applications in flexible and transparent electronic devices.¹²

In this paper, we investigate the intrinsic stochasticity of the resistive switching phenomenon in lateral SiO_x-based resistive switches, where the active volume is confined under graphene nanogaps. In similar device geometries, transmission electron microscopy (TEM) measurements demonstrated that the formation and degradation of discrete Si nanocrystals is a

Received: February 16, 2022

Accepted: April 25, 2022

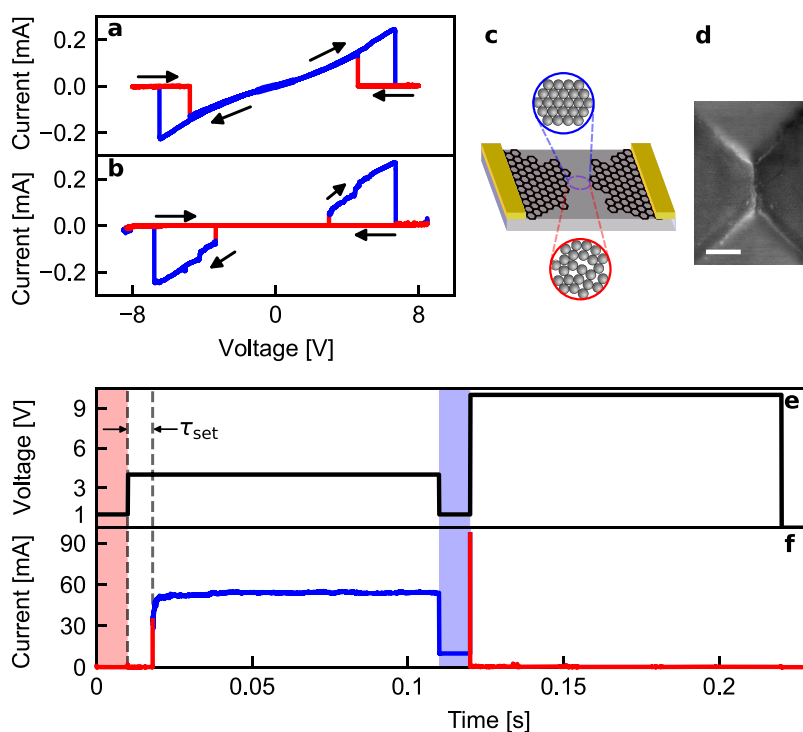


Figure 1. Resistive switching phenomenon in graphene/SiO_x/graphene nanogap devices. (a) Different $I(V)$ characteristics are observable when the period of the driving signal is tuned compared to τ_{dead} . For the upper curve a, the period of the driving signal is $T = 6$ s, and for the lower curve b, $T = 1$ s. (c) Schematics of the lateral graphene/SiO_x/graphene nanogap devices contacted with gold electrodes. The crystalline nature of the ON state and the amorphous nature of the OFF state are schematically illustrated. (d) Scanning electron microscopy image of a graphene/SiO_x/graphene nanogap device; scale bar: 200 nm. (e, f) Typical response of the device in pulsed measurements, showing the driving rectangular voltage signal (e, black curve) and the current versus time (f). Red/blue coloring of the traces corresponds to OFF/ON states of the device, and red/blue shaded areas mark the regions where the low bias OFF/ON resistances are recorded, respectively.

key ingredient of the switching process.^{13,14} In situ HRTEM analysis also indicated the presence of semimetallic crystalline Si-III phase in the low-resistance state (LRS, ON state),¹⁵ which is replaced by an amorphous, poorly conducting active region in the high-resistance state (HRS, OFF state).

In our previous work, we have introduced a technique for creating ultrasmall, truly \sim nm-sized graphene/SiO_x/graphene nanogap devices via the fine-controlled electrical breakdown of a graphene nanowire on the top of a SiO_x substrate.¹⁶ We anticipate that this device geometry is able to address a single or a few Si nanocrystals in the active volume. Here, we investigate the formation dynamics of such nanocrystals by investigating the set time values, i.e., the timespan between the programming pulse edge and the actual transition from the HRS to the LRS. Going beyond the investigation of average set time characteristics, and studying the entire statistical distribution of the stochastic set time of the graphene/SiO_x/graphene devices in the framework of nucleation theory, we gain fundamental information about the nanocrystal formation mechanism. Furthermore, we demonstrate that besides the obvious voltage dependence, the set time statistics are also sensitive to the nanostructure of the initial high-resistance state, which may vary along subsequent switching events, and which is intentionally tunable by the amplitude of the reset operation.

RESULTS AND DISCUSSION

The graphene/SiO_x/graphene PCM devices are established by the following fabrication steps: (i) A graphene nanowire is patterned on a SiO₂ substrate. (ii) A nanometer-scale gap is

established in the graphene wire by a fine, feedback-controlled electrical breakdown procedure (see Figure 1d). The analysis of the voltage-dependent tunneling current in our previous studies has demonstrated that in the narrowest region, the distance between the two graphene electrodes is in the range of ≈ 1 –3 nm. This allows us to confine the resistive switching to a much smaller active volume than in conventional nanofabricated devices, or in the case of uncontrolled breakdown. (iii) Finally, the resistive switching region under the graphene nanogap is electroformed. Previous TEM investigations have demonstrated that the electroformation is already accompanied by the formation of Si nanocrystals due to the SiO_x \rightarrow Si reduction process and oxygen migration.¹⁵ Note that the vacuum environment hinders the back-oxidation of the nanocrystals. More details on the fabrication procedure are available in our previous papers^{16–19} and in the Experimental Section.

Resistive switching phenomenon in the graphene/SiO_x/graphene nanogap devices leads to a broad range of analog states spanning several orders of magnitudes in resistance^{12,20,21} ($\approx 10^4$ – 10^{11} Ω). The set (OFF \rightarrow ON) and reset (ON \rightarrow OFF) processes are characterized by the τ_{set} and τ_{reset} switching times. Further dynamical properties emerge from an interplay of τ_{set} and the so-called dead time¹⁶ (τ_{dead}), which means that after a successful reset event, the device cannot be set to the ON state again for τ_{dead} characteristic time. This phenomenon leads to rather different $I(V)$ characteristics upon driving with symmetric triangular voltage signals of different period (T). The set and reset processes are considered to be driven by two fundamentally different

physical processes: electric field-aided crystallization and voltage-induced, self-heating-driven amorphization.^{15,16} Both processes are independent of the polarity of the applied voltage. At slow enough driving ($T \gg \tau_{\text{dead}}$), this yields a symmetric $I(V)$ curve (Figure 1a), where the initial ON state switches to the OFF state at V_{reset} , but along the backward sweep, the device switches back to the ON state at a smaller voltage (V_{set}), i.e., the OFF state is not available at zero bias. However, if T is chosen such that the set process remains prohibited until the end of the first half period, the device is stuck in the OFF state as the voltage is released (Figure 1b). This means that by proper driving, both the ON and OFF states can be programmed such that these are retained at zero bias. Note that this type of unipolar switching is characteristic to surface structures in vacuum environment, and this process clearly differs from alternative bulk intrinsic or extrinsic resistive switching processes of SiO_x ,¹¹ where bipolar characteristics are also possible.

Mapping device characteristics via pulsed measurement schemes are necessary for applications where interconnected memristive elements are programmed,^{3,22} or if the switching times are investigated. The basic pulsed programming scheme of our study is illustrated in Figure 1e,f. The device is prepared in the OFF state (red line in Figure 1f). A set pulse with $V_{\text{set}} = 4$ V switches the device to the ON state (blue line). Note that the set transition occurs with a definite time delay compared to the rising edge of the set pulse, which defines the set time. After releasing the set pulse, the device stays in the ON state until the subsequent reset pulse ($V_{\text{reset}} > 5$ V), which occurs with τ_{reset} time delay after the rising edge. The time scales of the set and reset processes are well tunable in the 10^0 – 10^{-8} s range via adjusting the amplitude of the programming voltage pulses. Note that in Figure 1f, τ_{reset} is so small that it is not resolved in the figure. The falling edge of the reset pulse is much shorter than $\tau_{\text{dead}} \approx 0.1$ – 1 s, i.e., after the reset pulse, the device stays in the OFF state until the pulse scheme is repeated. Prior to the set and reset pulses, a lower readout voltage (1 V) is applied to measure the low bias OFF and ON resistance in the time intervals with red and blue backgrounds in Figure 1e,f. The current response to the voltage driving is measured by a custom-built multiple-output current-to-voltage converter,²³ which enables real-time monitoring of the >4 orders of magnitude different ON and OFF resistances through parallel output channels with different amplification factors, i.e., there is no need for slow gain switching (see the Experimental Section for further details). The OFF (ON) state resistances are determined by measuring the current response through a high (low) gain output of the multiple-output current-to-voltage converter and averaging the such measured current values along the red (blue) readout regions in Figure 1e,f.

The set time statistics are studied in continuously cycled measurements according to the pulsed scheme shown in Figure 1e,f. The cycling period of these kinds of signals was usually set to 6–10 s $\gg \tau_{\text{dead}}$. A statistical analysis of the R_{OFF} , R_{ON} resistances of both the states and the τ_{set} set time was performed on multiple samples relying on several switching cycles. We found that at a given driving condition (i.e., at well-defined set and reset pulse amplitude and length), the endurance of the sample was in the range of 10^3 ,¹⁶ afterward, the modification of the driving parameters, e.g., the elevation of the reset pulse amplitude, is necessary to establish further

switching events. This way 1–2 orders of magnitude larger endurance is obtained until the complete failure.

In the following, we analyze the set time statistics along such homogeneously driven cycles and compare the results to the expectations of nucleation theory along the following considerations. The formation dynamics of the Si nanocrystals can be dominated by either a stochastic nucleation process or a deterministic growth process.^{10,24} Though in situ TEM measurements implied the transition between amorphous and crystalline Si phases,¹⁵ the role of oxygen migration in the switching process also cannot be excluded. As a comparison basis, in common nanoscale $\text{Ge}_2\text{Sb}_2\text{Te}_3$ (GST) phase change memory devices, the growth from the embedding crystalline matrix is considered a key ingredient of the set transition. In SiO_x devices, however the embedding matrix is amorphous, and the extremely small active volume of our devices reduces the chance for the presence of crystalline seeds in the as-quenched OFF state and therefore the emergence of nucleation seeds is considered as a prerequisite of the set transition. On the other hand, once a nucleation seed is formed, the subsequent growth time is expected to be extremely small due to the nanometer-scale volume. We note, however, that the growth from smaller residual Si nanocrystals in the HRS cannot be fully excluded. These considerations imply that the set process is rather dominated by the nucleation time in our devices. This is further supported by the nature of the set process: after the rising edge of the set pulse, an abrupt transition is observed; however, this is significantly delayed from the pulse edge (see Figure 1e,f and ref 16). Such a time-delayed abrupt transition is characteristic to a nucleation-driven process, whereas a growth-driven process should exhibit a gradual resistance increase, as reported in GST devices.²⁵

In a nucleation-driven process, the set time is well approximated by the nucleation time. The latter is considered as a stochastic variable following an exponential probability density function with an expectation value of $\bar{\tau}_{\text{nucleation}} \sim \exp(W/k_B T)$,^{26,27} where W is the effective nucleation barrier.²⁸ The field-induced nucleation model considers that along the set operation, the nucleation barrier breaks down^{26,27} due to the applied voltage, and therefore the set process exponentially speeds up as the set voltage is linearly increased, in agreement with the experimentally measured voltage dependence of the average set time.¹⁶ Theoretical calculations have shown that the electric field necessary to induce an amorphous to crystalline set transition is in the order of 300 MV/m,²⁹ which is a reasonable value in our devices with sub-10 nm-sized active volume.

To further check the validity of the nucleation model, we measured the set time values along several consecutive switching cycles and fitted the such acquired set time histograms by the prediction of nucleation theory, i.e., by an exponential probability density function. The latter density function has a unique property: regardless of the mean set time, the $\log_{10}(\tau_{\text{set}})$ values should exhibit a universal standard deviation, $\sigma_{\log(\tau)}^{\text{exponential}} = \pi/(\ln(10) \cdot \sqrt{6}) \approx 0.56$. This means that the standard deviation of $\log_{10}(\tau_{\text{set}})$ should always span around a half-order of magnitude along the time axis. A significantly smaller standard deviation would contradict the nucleation model, whereas a larger standard deviation would imply the presence of further stochasticity, like the cycle-to-cycle variation of the W nucleation barrier.

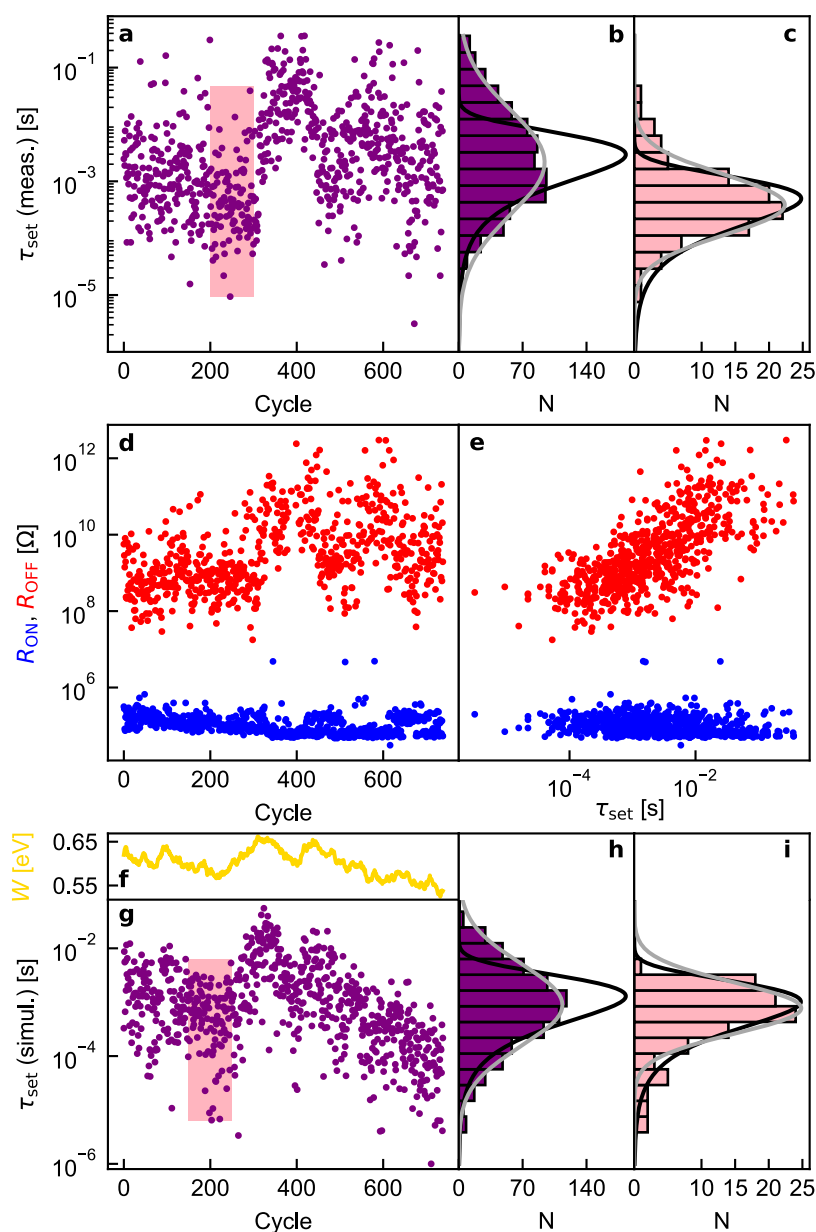


Figure 2. Measured and simulated set time statistics. (a) Set time values for 700 consecutive switching cycles and (b) the set time histogram for the same dataset (purple) together with the best fitting exponential (black) and lognormal (gray) probability density functions. (c) Set time distribution for a restricted, temporally homogeneous subset of the data (cycles with pink background in (a)). For this data subset, the set time histogram (pink) is similarly well fitted with the exponential (black) and lognormal (gray) probability density functions. (d) Evolution of the R_{OFF} and R_{ON} resistances for the same 700 cycles. (e) ON and OFF resistance values as a function of τ_{set} in the same cycle. The OFF (ON) resistances are well correlated with (independent of) the set time. (f–i) Results of the simulation where the set transition is modeled as a nucleation process with a ΔW variation of the nucleation barrier around its mean value, \bar{W} , setting a dedicated correlation cycle number (n_{corr}) (f); (g) shows the such simulated set time values for 700 cycles together with the set time histograms for the entire simulated dataset (h) and the restricted, temporally homogeneous dataset (pink background in (g) and pink histogram in (i)). Both set time histograms are fitted by exponential (black) and lognormal (gray) probability density functions.

Figure 2a–e shows an example set of measurements including 700 consecutive switching cycles. Figure 2b shows the histogram of the measured set time values (note the logarithmic axis) together with the best fitting exponential probability density function (black line; see the detailed fitting formula in the Experimental Section). It is clear that the measured set time distribution is significantly wider than the best fitting exponential probability density function: the $\sigma_{\log(\tau)}^{\text{measured}} \approx 0.87$ standard deviation value is significantly larger than the universal $\sigma_{\log(\tau)}^{\text{exponential}} \approx 0.56$ value. Instead, a lognormal

distribution (see the gray line in Figure 2b and the detailed fitting formula in the Experimental Section) properly describes the data suggesting that multiple characteristic time scales are present in the system. (Note that the standard deviation of $\log_{10}(\tau_{\text{set}})$ for the best fitting lognormal density function, $\sigma_{\log(\tau)}^{\text{lognormal}} \approx 0.91$ indeed describes a similarly wide distribution as the measured histogram.)

The cycle-to-cycle variation of the set time in Figure 2a clarifies that the broad set time distribution is not related to a temporally homogeneous dataset, rather a significant drifting of

the average set time is observed on the time scale of ≈ 100 – 200 cycles. In this context, it is also useful to investigate the set time distribution for a statistically more homogeneous portion of the data, like the 100 datapoints with pink background. For this restricted dataset, the exponential and lognormal probability density functions display similarly good fitting curves to the experimental set time distribution (see the measured set time histogram and the best fitting curves for this data subset in Figure 2c). For this restricted dataset, the measured standard deviation is $\sigma_{\log(\tau)}^{\text{measured}} \approx 0.61$, which is still slightly larger than the universal $\sigma_{\log(\tau)}^{\text{exponential}} \approx 0.56$ value, the latter, however, coincides with the standard deviation of the best fitting lognormal distribution, $\sigma_{\log(\tau)}^{\text{lognormal}} \approx 0.56$. It can be generally stated that for temporally homogeneous portions of the data, the $\sigma_{\log(\tau)}^{\text{measured}}$ values are less than 20% larger than the universal $\sigma_{\log(\tau)}^{\text{exponential}}$ value, and therefore the exponential distribution reasonably fits the measured set time histograms.

All of these imply that on a shorter term, the set time distribution is indeed reasonably well described by nucleation theory considering a constant $W(V_{\text{set}})$ nucleation barrier at the given set voltage. However, after a characteristic number of ≈ 100 – 200 cycles, the nucleation barrier of the OFF state is randomly drifting. As the set time exponentially depends on W , a relatively small ΔW cycle-to-cycle variation of the nucleation barrier yields a significant broadening of the set time distribution.

The temporal inhomogeneity of the set time can be also mimicked by numerical simulations considering (i) an exponential probability density function of the set time at a certain nucleation barrier (W) and (ii) a random temporal variation of the nucleation barrier with a certain ΔW variance and a dedicated correlation time such that the switching cycle number-dependent $\langle W(n) \cdot W(n + \Delta n) \rangle$ correlation function decays on the scale of $\Delta n \approx n_{\text{corr}}$ switching cycles. An accordingly simulated example set time variation is demonstrated in Figure 2f–i (see the Experimental Section for more details on the simulation). This simulation with an average nucleation barrier of $\bar{W} = 0.62$ eV, a standard deviation of $\Delta W = 0.04$ eV, and a correlation time of $n_{\text{corr}} = 200$ cycles very well resembles the experimental data in Figure 2a–e. The minor cycle-to-cycle variation of the W nucleation barrier ($\Delta W/\bar{W} = 6.5\%$, see Figure 2f) converts to orders of magnitude variation of the set time (Figure 2g), yielding a broadened lognormal set time distribution at cycle numbers significantly exceeding $n_{\text{corr}} = 200$. This is demonstrated in Figure 2h showing the set time histogram for the entire simulated dataset in Figure 2g ($\sigma_{\log(\tau)}^{\text{simulated}} \approx 0.77$) together with the best fitting lognormal (gray, $\sigma_{\log(\tau)}^{\text{simulated}} \approx 0.77$) and exponential (black) probability density functions. However, for a smaller number of cycles, a temporally more homogeneous set time variation is observed (see, e.g., the 100 switching cycles with pink background in Figure 2g), where the set time distribution is well described by an exponential probability density function with a single W nucleation barrier. The latter is illustrated in Figure 2i, where the histogram shows the set time distribution for the pink region in Figure 2g ($\sigma_{\log(\tau)}^{\text{simulated}} \approx 0.62$) together with the best fitting exponential and lognormal probability density functions ($\sigma_{\log(\tau)}^{\text{lognormal}} \approx 0.48$).

All of these measurements and simulations are in sharp contrast to mushroom-type GST-based memory devices, where the measured set time distribution is not wider but rather significantly narrower than the universal exponential distribution. (According to our rough estimate, the data in

Figure 11b of ref 10 reflect 3–10 times smaller $\sigma_{\log(\tau)}^{\text{measured}}$ values than the universal $\sigma_{\log(\tau)}^{\text{exponential}}$ value.) This comparison confirms that the set time in the latter GST devices is indeed dominated by a more deterministic growth process, whereas in our devices, the set time distribution is consistent with a stochastic nucleation-driven process with a significant variation of the nucleation barrier on the scale of 100–200 switching cycles.

It is also interesting to analyze how the ON and OFF state resistances vary along the same 700 switching cycles of Figure 2a and to what extent these resistances are correlated with the actual set time values. Figure 2d demonstrates that R_{ON} (blue curve) exhibits minor temporal inhomogeneities, whereas R_{OFF} displays significant temporal variations with a similar pattern to τ_{set} (Figure 2a). Figure 2e shows the ON and OFF state resistances as a function of the set time in the same cycle, demonstrating the lack of correlation between R_{ON} and τ_{set} and very significant correlation between R_{OFF} and the set time. This finding indicates that the OFF state resistance and the related detailed nanostructure of the active volume in the HRS are not stable in time, rather exhibit temporal variations on the time scale of 100–200 cycles. Such variation can be caused by, e.g., the random structure of atomic configurations of the amorphous region after each reset event,¹⁰ or the variation of the effective active volume's size, which perturbs the length scale at which the voltage drops on the HRS. This variation is mirrored in the temporal inhomogeneity of the set time via the variation of the nucleation barrier according to the actual nanostructure of the HRS. Similar findings were observed along several switching cycles recorded on various samples.

The observed correlation between the R_{OFF} and τ_{set} quantities (see Figure 2e) suggests that the tuning of the τ_{set} statistics could be viable with the variation of the V_{reset} amplitude since the latter could act as a control parameter for tuning the R_{OFF} resistances along with the τ_{set} set times. To study the controllability of the set time statistics, we investigated the effects of tuning the reset voltage amplitude while other parameters of the driving voltage signal were kept constant. To eliminate drift phenomena (illustrated in Figure 2a), the effects of changing V_{reset} were studied within the correlation cycle number, for an overall ≈ 200 cycles, as seen in Figure 3a,b. Both of the expectation value of τ_{set} and the expectation value of the logarithm of R_{OFF} (see lines on datapoints in Figure 3a,b) increase with increasing V_{reset} from 8.5 to 10 V, and resume to their initial values when V_{reset} is decreased back. Besides that, the expectation value of R_{ON} remains constant through the cycles. These tendencies are even better visualized by plotting the expectation values of the logarithm of the ON and OFF state resistances and the set time against the V_{reset} reset voltage (see Figure 3c,d). It is clear that R_{OFF} (red points in Figure 3c) and accordingly τ_{set} (Figure 3d) are well tunable by the reset voltage, whereas R_{ON} remains independent of V_{reset} . These dependencies yield a very similar correlation plot between τ_{set} and R_{ON} or R_{OFF} as the one previously observed in Figure 2e; however, in this case (Figure 3e), the correlated variation of the set time and the OFF resistance is not related to a random drift, but it is intentionally induced by the proper setting of the reset voltage. These findings underpin that the nanostructure of the high-resistance state, and thereby the time scale of the subsequent set operation are well tunable by the amplitude of the reset operation.

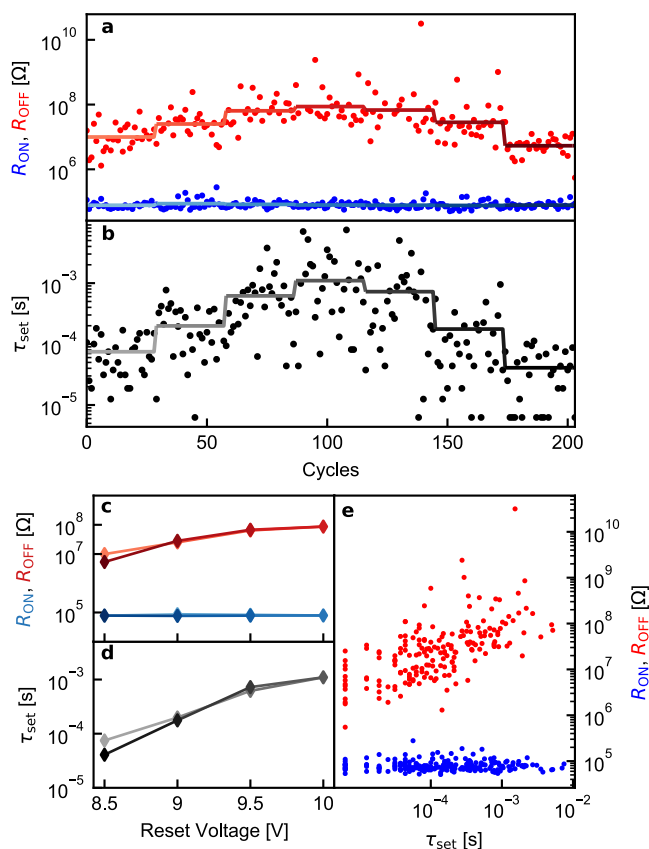


Figure 3. Tuning the distributions of the set time and the OFF state resistance with the variation of the reset voltage amplitude. (a, b) ON and OFF state resistances with respect to the cycle number. Set pulse amplitude and length are kept constant, $V_{\text{set}} = 4$ V throughout the measurement, and reset amplitude is varied every 10 cycles in 0.5 V steps, from 8.5 to 10 V and back to 8.5 V again. The solid lines represent the logarithmically averaged values for the cycles with constant V_{reset} . (c) Expectation values of the logarithm of ON and OFF state resistances and (d) the set time, where color shading from lighter to darker markers/lines reflect the order of the measurements similarly to (a) and (b). (e) OFF/ON state resistances as a function of the set time exhibit correlation/independent behavior accordingly.

CONCLUSIONS

In conclusion, we have studied the formation dynamics of Si nanocrystals in the active volume of graphene–SiO_x–graphene resistive switching devices by (i) investigating the entire statistical distribution of the set time values and (ii) studying the tunability of the set time via the manipulation of the HRS. We found that in a shorter set of switching cycles, the measured set time distribution is well fitted by an exponential probability density function describing a nucleation process with constant nucleation barrier and exhibiting a universal standard deviation of the $\log_{10}(\tau_{\text{set}})$ values. This finding underpins the nucleation-dominated nature of the set process, which is in sharp contrast to the growth-dominated set process in GST devices, the latter exhibiting a significantly narrower set time distribution. For a longer set of switching cycles, our measurements exhibit an even wider set time distribution, which is related to the cycle-to-cycle variation of the W nucleation barrier height with a typical correlation parameter of $n_{\text{corr}} \approx 200$ switching cycles. We found that the latter temporal variation of the average set time is very well correlated with the OFF state resistance of the device before

the actual set transition, i.e., the cycle-to-cycle variation of the nucleation barrier is related to the cycle-to-cycle variation of the actual nanostructure of the HRS. Furthermore, we found that the nanostructure of the HRS and thereby the average set time is not only spontaneously varying from cycle to cycle, but it can also be intentionally manipulated by changing the amplitude of the reset voltage pulse. These results contribute to the fundamental understanding of the stochastic switching process in surface-based SiO_x resistive switches, as well as to the design of two-dimensional circuits, where the graphene–SiO_x–graphene structures can serve as easily embeddable analog memory elements with stochastic switching characteristics. Such tunable stochastic properties can serve as a basis for the realization of neuronal activation functions,³⁰ stochastically firing neurons or energy-efficient true random number generation³¹

EXPERIMENTAL SECTION

Fabrication of Graphene/SiO_x/Graphene Nanogap Devices.

The large-area single-layer graphene sheet was grown on copper foil using chemical vapor deposition in a low-pressure furnace. The graphene was transferred by the wet etching method onto a Si substrate covered by 300 nm thick thermal oxide. The Ti/Au electrodes were defined by electron-beam lithography and deposited by electron-beam evaporation. The graphene sheet was tailored into 200 nm wide bow-tie-shaped constrictions using another lithography process and Ar/O₂ plasma etching. The few-nanometers-sized gaps were formed by a controlled electrical breakdown procedure, applying a gradually increasing pulsed signal to the graphene nanostripes, maintaining continuous feedback to the resistance, as described in ref 16.

Multiple-Output Current-to-Voltage Converter. During the set/reset process of PCMs, the current changes many orders of magnitude in a short time, which requires an extremely high dynamic range and fast response. The multiple-output linear current-to-voltage converter, owing to its special circuit diagram,²³ enables us to measure the current from picoamperes to milliamperes range. The amplification of the five different channels varies between 10³ and 10⁸ V/A. The bandwidth of the most sensitive channel is 4 kHz, while the lowest amplification has a few hundreds of kHz cutoff frequency. Simultaneously sampling all of the five channels, the current–time characteristic of the switching can be merged with high resolution covering a very broad current range. In these specific set time measurements, the ON and OFF resistances were, respectively, measured through two parallel output channels with 1.8×10^4 V/A and 10⁸ V/A amplification.

Fitting of the Measured Set Time Distribution. Curve fitting is done to logarithmically spaced histogram data, applying the appropriate transformation of exponential and lognormal functions.³² In this manner, the exponential fitting function is

$$\rho_{\text{exp}}(t) = A\lambda \cdot e^{-\lambda t} \quad (1)$$

where A and λ are the fit parameters. Similarly, the lognormal fitting function is

$$\rho_{\text{log-norm}}(t) = \frac{A}{w\sqrt{\pi}t} \cdot \exp\left\{-\frac{1}{w^2} \ln\left(\frac{t}{t_0}\right)^2\right\} \quad (2)$$

where A , w , and t are the fit parameters.

Simulation of the Set Time Series. To mimic the inhomogeneous region of set times (like the random drifting of the average set time in the entire dataset of Figure 2a), we assume a cycle number-dependent variation for the W nucleation barrier parameter, an equivalent of a low-pass filtered white noise, or the so-called Ornstein–Uhlenbeck process.³³ In this manner, the nucleation barrier in the $n + 1$ cycle is calculated as

$$W_{n+1} = W_n - \frac{1}{n_{\text{corr}}}(W_n - \bar{W}) + \xi(\sigma_{\Delta W}, n) \quad (3)$$

where $\bar{W} = 0.62$ eV is the average nucleation barrier and $n_{\text{corr}} = 200$ is the correlation cycle number. $\xi(\sigma_{\Delta W}, n) = \mathcal{N}(0, \sigma_{\Delta W})$ is a Gaussian random variable with zero expectation value and $\sigma_{\Delta W} = 0.004$ eV standard deviation. \bar{W} and $\sigma_{\Delta W}$ are chosen such that the set time values according to the formula $\bar{\tau}_{\text{set}} = \bar{\tau}_{\text{nucleation}} \approx \tau_0 \exp(W/k_B T)$ should resemble the experimental data presented in Figure 2a. Note that the τ_0 attempt frequency is approximated as a typical phonon frequency, $\tau_0 \sim 10^{-13}$ s.^{26,27}

AUTHOR INFORMATION

Corresponding Author

András Halbritter – Department of Physics, Institute of Physics, Budapest University of Technology and Economics, H-1111 Budapest, Hungary; MTA-BME Condensed Matter Research Group, H-1111 Budapest, Hungary; Email: halbritter.andras@ttk.bme.hu

Authors

Tímea Nóra Török – Department of Physics, Institute of Physics, Budapest University of Technology and Economics, H-1111 Budapest, Hungary; Institute of Technical Physics and Materials Science, Centre for Energy Research, 1121 Budapest, Hungary

János Gerő Fehérvári – Department of Physics, Institute of Physics, Budapest University of Technology and Economics, H-1111 Budapest, Hungary

Gábor Mészáros – Research Centre for Natural Sciences, Institute of Materials and Environmental Chemistry, Eötvös Lóránd Research Network, 1117 Budapest, Hungary

László Pósa – Department of Physics, Institute of Physics, Budapest University of Technology and Economics, H-1111 Budapest, Hungary; Institute of Technical Physics and Materials Science, Centre for Energy Research, 1121 Budapest, Hungary; orcid.org/0000-0001-7303-4031

Complete contact information is available at: <https://pubs.acs.org/10.1021/acsnm.2c00722>

Author Contributions

[†]T.N.T. and J.G.F. contributed equally to this work. The nanogap devices were developed and prepared by L.P. The measurements and the data analysis were performed by T.N.T. and J.G.F. The manuscript was written by T.N.T. and A.H. The multiple-output current-to-voltage converter was designed and prepared by G.M. The project was supervised by A.H. and L.P.

Notes

The authors declare no competing financial interest.

ACKNOWLEDGMENTS

This work was supported by the Ministry for Innovation and Technology and the National Research, Development and Innovation Office within the Quantum Information National Laboratory of Hungary, and the NKFI K128534 grant. T.N.T. acknowledges the support of the KDP-2020 963575 Cooperative Doctoral Programme of the Ministry for Innovation and Technology, and L.P. acknowledges the support of the ÚNKP-21-4 new national excellence program of the Ministry for Innovation and Technology from the source of the National Research, Development and Innovation Fund.

REFERENCES

- Zidan, M. A.; Strachan, J. P.; Lu, W. D. The future of electronics based on memristive systems. *Nat. Electron.* **2018**, *1*, 22–29.
- Xia, Q.; Yang, J. J. Memristive crossbar arrays for brain-inspired computing. *Nat. Mater.* **2019**, *18*, 309–323.
- Ambrogio, S.; Narayanan, P.; Tsai, H.; Shelby, R.; Boybat, I.; Nolfo, C.; Sidler, S.; Giordano, M.; Bodini, M.; Farinha, N.; Killeen, B.; Cheng, C.; Jaoudi, Y.; Burr, G. Equivalent-accuracy accelerated neural-network training using analogue memory. *Nature* **2018**, *558*, 60–67.
- Li, C.; Han, L.; Jiang, H.; Jang, M. H.; Lin, P.; Wu, Q.; Barnell, M.; Yang, J. J.; Xin, H.; Xia, Q. Three-dimensional crossbar arrays of self-rectifying Si/SiO₂/Si memristors. *Nat. Commun.* **2017**, *8*, No. 15666.
- Wang, Z.; Li, C.; Lin, P.; Rao, M.; Nie, Y.; Song, W.; Qiu, Q.; Li, Y.; Yan, P.; Strachan, J. W.; Ge, N.; McDonald, N.; Wu, Q.; Hu, M.; Wu, H.; Williams, S.; Xia, Q.; Yang, J. J. In situ training of feed-forward and recurrent convolutional memristor networks. *Nat. Mach. Intell.* **2019**, *1*, 434–442.
- Cai, F.; Kumar, S.; Vaerenbergh, T.; Sheng, X.; Liu, R.; Li, C.; Liu, Z.; Foltin, M.; Yu, S.; Xia, Q.; Yang, J. J.; Beausoleil, R.; Lu, W.; Strachan, J. W. Power-Efficient combinatorial optimization using intrinsic noise in memristor Hopfield neural networks. *Nat. Electron.* **2020**, *3*, 1–10.
- Mahmoodi, M. R.; Prezioso, M.; Strukov, D. B. Versatile stochastic dot product circuits based on non-volatile memories for high performance neurocomputing and neurooptimization. *Nat. Commun.* **2019**, *10*, No. 5113.
- Borders, W. A.; Pervaiz, A. Z.; Fukami, S.; Camsari, K. Y.; Ohno, H.; Supriyo, D. Integer factorization using stochastic magnetic tunnel junctions. *Nature* **2019**, *573*, 390–393.
- Ielmini, D.; Waser, R.; Akinaga, H. *Resistive Switching: From Fundamentals of Nanoionic Redox Processes to Memristive Device Applications*, Wiley-VCH: Germany, 2016.
- Le Gallo, M.; Sebastian, A. An overview of phase-change memory device physics. *J. Phys. D: Appl. Phys.* **2020**, *53*, No. 213002.
- Mehonic, A.; Shluger, A.; Gao, D.; Valov, I.; Miranda, E.; Ielmini, D.; Bricalli, A.; Ambrosi, E.; Li, C.; Yang, J. J.; Xia, Q.; Kenyon, A. Silicon Oxide (SiO_x): A Promising Material for Resistance Switching? *Adv. Mater.* **2018**, *30*, No. 1801187.
- Yao, J.; Lin, J.; Dai, Y.; Ruan, G.; Yan, Z.; Li, L.; Zhong, L.; Natelson, D.; Tour, J. M. Highly transparent non-volatile resistive memory devices from silicon oxide and graphene. *Nat. Commun.* **2012**, *3*, No. 1101.
- Yao, J.; Sun, Z.; Zhong, L.; Natelson, D.; Tour, J. Resistive Switches and Memories from Silicon Oxide. *Nano Lett.* **2010**, *10*, 4105–4110.
- He, C.; Li, J.; Wu, X.; Chen, P.; Zhao, J.; Yin, K.; Cheng, M.; Yang, W.; Xie, G.; Wang, D.; Liu, D.; Yang, R.; Shi, D.; Li, Z.; Sun, L.; Zhang, G. Tunable Electroluminescence in Planar Graphene/SiO₂ Memristors. *Adv. Mater.* **2013**, *25*, 5593–5598.
- Yao, J.; Zhong, L.; Natelson, D.; Tour, J. In Situ Imaging of the Conducting Filament in a Silicon Oxide Resistive Switch. *Sci. Rep.* **2012**, *2*, No. 242.
- Posa, L.; Abbassi, M.; Makk, P.; Santa, B.; Nef, C.; Csontos, M.; Calame, M.; Halbritter, A. Multiple physical timescales and dead time rule in fewnm sized graphene-SiO_x-graphene memristors. *Nano Lett.* **2017**, *17*, 6783–6789.
- Nef, C.; Pósa, L.; Makk, P.; Fu, W.; Halbritter, A.; Schönenberger, C.; Calame, M. High-yield fabrication of nmsize gaps in monolayer CVD graphene. *Nanoscale* **2014**, *6*, 7249–7254.
- El Abbassi, M.; Pósa, L.; Makk, P.; Nef, C.; Thodkar, K.; Halbritter, A.; Calame, M. From electroburning to sublimation: substrate and environmental effects in the electrical breakdown process of monolayer graphene. *Nanoscale* **2017**, *9*, 17312–17317.
- Pósa, L.; Balogh, Z.; Krisztián, D.; Balázs, P.; Sánta, B.; Furrer, R.; Csontos, M.; Halbritter, A. Noise diagnostics of graphene interconnects for atomic-scale electronics. *npj 2D Mater. Appl.* **2021**, *5*, No. 57.

(20) He, C.; Shi, Z.; Zhang, L.; Yang, W.; Yang, R.; Shi, D.; Zhang, G. Multilevel resistive switching in planar graphene/SiO₂ nanogap structures. *ACS Nano* **2012**, *6*, 4214–4221.

(21) Fowler, B. W.; Chang, Y.-F.; Zhou, F.; Wang, Y.; Chen, P.-Y.; Xue, F.; Chen, Y.-T.; Bringhurst, B.; Pozder, S.; Lee, J. C. Electroforming and resistive switching in silicon dioxide resistive memory devices. *RSC Adv.* **2015**, *5*, 21215–21236.

(22) Boybat, I.; Le Gallo, M.; Nandakumar, S. R.; Moraitis, T.; Parnell, T.; Tuma, T.; Rajendran, B.; Leblebici, Y.; Sebastian, A.; Eleftheriou, E. Neuromorphic computing with multi-memristive synapses. *Nat. Commun.* **2018**, *9*, No. 2514.

(23) Mészáros, G.; Li, C.; Pobelov, I.; Wandlowski, T. Current measurements in a wide dynamic range - Applications in electrochemical nanotechnology. *Nanotechnology* **2007**, *18*, No. 424004.

(24) Zhang, W.; Mazzarello, R.; Wuttig, M.; Ma, E. Designing crystallization in phasechange materials for universal memory and neuro-inspired computing. *Nat. Rev. Mater.* **2019**, *4*, 150–168.

(25) Le Gallo, M.; Athmanathan, A.; Krebs, D.; Sebastian, A. Evidence for thermally assisted threshold switching behavior in nanoscale phase-change memory cells. *J. Appl. Phys.* **2016**, *119*, No. 025704.

(26) Karpov, V. G.; Kryukov, Y. A.; Mitra, M.; Karpov, I. V. Crystal nucleation in glasses of phase change memory. *J. Appl. Phys.* **2008**, *104*, No. 054507.

(27) Karpov, V. G.; Kryukov, Y. A.; Karpov, I.; Karpov, I. V.; Mitra, M. Fieldinduced nucleation in phase change memory. *Phys. Rev. B* **2008**, *78*, No. 052201.

(28) Kohary, K.; Wright, C. D. Electric field induced crystallization in phase-change materials for memory applications. *Appl. Phys. Lett.* **2011**, *98*, No. 223102.

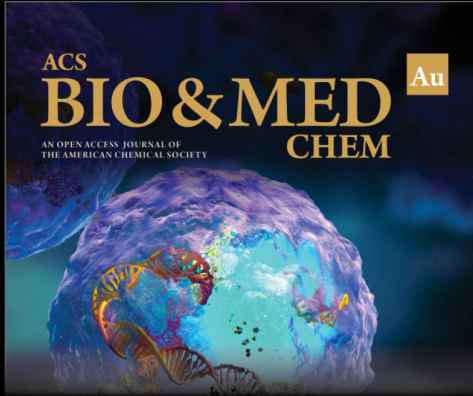
(29) Vázquez Diosdado, J. A.; Ashwin, P.; Kohary, K. I.; Wright, C. D. Threshold switching via electric field induced crystallization in phase-change memory devices. *Appl. Phys. Lett.* **2012**, *100*, No. 253105.

(30) Shin, J. H.; Jeong, Y. J.; Zidan, M. A.; Wang, Q.; Lu, W. D. In *Hardware Acceleration of Simulated Annealing of Spin Glass by RRAM Crossbar Array*, IEEE International Electron Devices Meeting (IEDM), 2018; pp 3.3.1–3.3.4.

(31) Sebastian, A.; Gallo, M.; Khaddam-Aljameh, R.; Eleftheriou, E. Memory devices and applications for in-memory computing. *Nat. Nanotechnol.* **2020**, *15*, 529–544.

(32) Nekola, J. C.; Sizling, A.; Boyer, A.; Storch, D. Artifacts in the Log- Transformation of Species Abundance Distributions. *Folia Geobot.* **2008**, *43*, 259–268.


(33) Bibbona, E.; Panfilo, G.; Tavella, P. The Ornstein-Uhlenbeck process as a model of a low pass filtered white noise. *Metrologia* **2008**, *45*, No. S117.




ACS
BIO & MED
AN OPEN ACCESS JOURNAL OF
THE AMERICAN CHEMICAL SOCIETY
CHEM
Au

Editor-in-Chief: **Prof. Shelley D. Minteer**, University of Utah, USA

Deputy Editor
Prof. Squire J. Booker
Pennsylvania State University, USA

Open for Submissions 

pubs.acs.org/biomedchemau  ACS Publications
Most Trusted. Most Cited. Most Read.